Research Square

Preprints are preliminary reports that have not undergone peer review.
They should not be considered conclusive, used to inform clinical practice,
or referenced by the media as validated information.

Research on damage characteristics and slope instability mechanism of loess under the wet-dry-freeze-thaw coupling cycles

Yuanpeng Cao
Northwest University
Xingang Wang
xgwangnwu@163.com

Northwest University

Research Article

Keywords: Wet-dry-freeze-thaw cycles, Loess, Shear behavior, Damage evolution, Mechanism analysis

Posted Date: October 27th, 2026

DOI: https://doi.org/10.21203/rs.3.rs-11487200/v1

License: This work is licensed under a Creative Commons Attribution 4.0 International License.
Read Full License

Additional Declarations: The authors declare no competing interests.

Research on damage characteristics and slope instability mechanism of loess under the wet-dry-freeze-thaw coupling cycles

Yuanpeng Cao [a, b, c], Xingang Wang [a, b, c *], Kai Liu [a, b, c], Jishi Geng [d], Baoqin Lian [a, b, c], Xu Zhou [a, b, c]

[a] State Key Laboratory of Continental Evolution and Early Life, Northwest University, Xi'an, Shaanxi 710069, China.

[b] Shaanxi Belt and Road Joint Laboratory on Special Geotechnical Dynamic Disaster Prevention, Xi'an, China.

[c] Digital Twin and Major Facility Disaster Prevention and Control Key Laboratory of Higher Education in Shaanxi Province, Northwest University, Xi'an, Shaanxi 710069, China.

[d] College of Geology and Environment, Xi'an University of Science and Technology, Xi'an 710054, China.

[*] Corresponding author: Xingang Wang [*]

✉ xgwangnwu@163.com

ABSTRACT

In recent years, the alternating changes in extreme climate have frequently caused loess to undergo the combined effects of wet-dry (WD) cycles and freeze-thaw (FT) cycles, leading to an increasing occurrence of overall instability and sliding in loess slopes. To reveal the damage mechanism of loess materials under the coupled wet-dry and freeze-thaw (WDFT) action and the evolutionary mechanism of landslides induced thereby, this study conducted a series of WD cycles, FT cycles, and WDFT coupling cycles tests. Multiple testing methods, including P-wave velocity, thermal conductivity, electrical resistivity, scanning electron microscopy and direct shear tests, were combined to systematically evaluate the evolution patterns of loess in terms of macroscopic physical-mechanical properties and microstructure. The results indicate that physical-mechanical properties attenuate nonlinearly with increasing cycles, driven by rising porosity and microstructural complexity, while the stress-strain behavior transitions from strong to weak strain softening. Due to distinct core mechanisms of cycle modes, their damage effects exhibit significant temporal and severity differences. In the early stages of cycling, the deterioration capability of FT action is greater than that of WD action; as the number of cycles increases, WD action becomes more significant. The damage to loess from the coupled WD and FT effects is not merely an additive combination of their individual effects but represents a more complex accelerating deterioration. For example, at 50 kPa, the final degradation rate of shear strength caused by WD, FT, and WDFT cycle modes are 0.64, 0.61, and 0.76, respectively. The WD cycles generate directional crack networks, FT cycles induce porous structures, and

WDFT coupling combines both into a more complex interconnected damage system. The WDFT coupling promotes a cross-scale failure process in loess, from microscopic damage to macroscopic slope instability, through a positive feedback mechanism involving crack network expansion and freeze-thaw fragmentation. This study provides important experimental data and a theoretical basis for an in-depth understanding of the disaster mechanisms and stability assessment of loess slopes under complex extreme environmental conditions.

Keywords: Wet-dry-freeze-thaw cycles; Loess; Shear behavior; Damage evolution; Mechanism analysis

1. Introduction

Loess, as a typical Quaternary sediment, covers approximately 10% of the global land area and is widely distributed in mid-latitude arid and semi-arid regions, such as Asia, Central Europe, and the mid-western part of North America [14, 20, 23, 31]. In China, loess is mainly distributed in the Loess Plateau and the Ili River Valley region [26, 32]. Influenced by transportation and deposition processes during geological history, these areas have formed numerous primary loess slopes [29, 34]. Furthermore, based on the principle of using locally available materials, loess has also been extensively used as fill material for infrastructure such as roadbeds and dams [18]. However, due to its characteristics of high porosity, low density, loose structure, and well-developed vertical joints, the mechanical properties of loess are highly sensitive to moisture changes and external loads. Under the influence of external factors such as temperature

differences and precipitation, it is prone to sudden failure, thereby inducing geological disasters like landslides, ground subsidence, and ground fissures, which seriously threaten engineering safety in loess regions [7, 13, 33, 47, 49, 50].

The deterioration of loess engineering performance is primarily attributed to natural environmental processes and human activities [17, 43]. In recent years, the increasing frequency of extreme climate events, such as high-temperature droughts, heavy rainfall, and cold waves, has led to alternating occurrences of these phenomena in the Loess Plateau region. Consequently, loess is subjected to a dynamic environment characterized by the intertwined effects of wet-dry (WD) and freeze-thaw (FT) cycles [4, 8, 28]. Research indicates that WD and FT cycles, driven by climatic conditions, are key factors accelerating structural damage and strength degradation in soil, significantly compromising the long-term structural stability and safety of infrastructure [1]. Numerous researchers have employed various techniques, including resistivity testing, permeability coefficient measurement, triaxial test, direct shear test, scanning electron microscopy (SEM), and nuclear magnetic resonance (NMR), to systematically analyze the evolution of the physical-mechanical properties and microstructure of loess under WD and FT cycles [16, 24, 30, 40]. Results demonstrate a general trend of progressive deterioration in parameters such as sample density, shear strength, and porosity after cyclic actions [22, 35, 37]. Although both WD and FT cycles significantly affect physical-mechanical properties, the extent of damage differs. For instance, some studies utilizing direct shear tests have found that both cohesion and the internal friction angle decay exponentially with increasing WD cycles before stabilizing.

In contrast, FT cycles primarily weaken cohesion, with a relatively smaller impact on the internal friction angle [21, 38]. This discrepancy stems from their distinct underlying mechanisms.

Numerous studies have demonstrated that WD cycles affect soil structure through the following mechanisms: moisture intrusion leads to the dissolution of cementing materials, weakening inter-particle bonds, while the hydration and swelling of clay minerals soften the soil structure [44]. During the drying and evaporation process, the generated shrinkage stress can induce desiccation cracks when it exceeds the tensile strength of soil [9]. The primary mechanism of FT cycles involves the frost heave stress generated by ice lenses during the freezing process, which alters the cementation state between particles. This leads to the fragmentation and reorganization of mineral particles and aggregates, generating new pores and causing the continuous extension of existing cracks [1, 36].

In summary, although extensive research has explored the effects of WD and FT cycles on the engineering properties of soils such as loess and significant progress has been made regarding the deterioration mechanisms under individual weathering processes, the actual damage accumulation and failure of loess materials in natural environments are often the result of the combined effects of wet-dry-freeze-thaw (WDFT) coupling due to complex and variable climatic conditions [5]. Existing studies have indicated that multidimensional deformation behaviors in geotechnical engineering, such as foundation heave or collapse, frequently originate from the synergistic action of WD and FT cycles. Microstructural damage induced by WD action

105 can be further exacerbated by subsequent FT processes, leading to a significant
106 reduction in the mechanical properties of soil after undergoing WDFT coupling cycles
107 [2, 48]. However, current experimental research on the deformation characteristics of
108 loess predominantly focuses on individual weathering processes. There remains a
109 notable deficiency in qualitatively and quantitatively elucidating the evolution of loess's
110 physical-mechanical properties under coupled WDFT cycles and the synergistic
111 mechanisms by which they induce slope instability.

112 This study conducts laboratory simulation tests to comparatively analyze the
113 evolution of physical parameters (P-wave velocity, thermal conductivity and electrical
114 resistivity) and mechanical indicators (shear strength, cohesion and internal friction
115 angle) of loess specimens under WD cycles, FT cycles and WDFT coupling cycles.
116 Through the qualitative and quantitative analysis of SEM tests, the microscopic
117 cooperative failure mechanism of WDFT coupling was clarified, thereby linking the
118 microscopic deterioration to the macroscopic slope instability. The practical
119 significance of this study lies in providing essential experimental data and a physical-
120 mechanical theoretical basis for the long-term stability evaluation and disaster
121 prediction of loess infrastructure under increasingly frequent extreme, alternating
122 climatic conditions. This study contributes to a deeper understanding of the damage
123 mechanism of loess materials under coupled WDFT effects. This study has certain
124 limitations. The experiments were conducted under controlled laboratory conditions,
125 which simplify the complex and natural conditions. Furthermore, given that this study
126 only focused on the loess in a specific area, subsequent research will concentrate on the

127 correlation between the small-scale indoor experiments and the large-scale model tests.
128 Through large-scale physical model tests or in-situ monitoring experiments at the site,
129 it will further reveal the impact of extreme environmental factors on the stability of
130 loess slopes.

131 **2. Materials and methods**

132 *2.1. Study area*

133 As shown in Fig. 1, the study area is located in Jingbian County, Yulin City, Shaanxi
134 Province, China. Field investigations revealed that the slopes in this area are
135 characterized by a thick loess overburden and complex engineering geological
136 conditions, with a wide distribution of human-made slopes. The study area experiences
137 a temperate semi-arid continental monsoon climate, featuring distinct precipitation and
138 evaporation periods, with relatively low annual precipitation and high evaporation rates.
139 According to meteorological data statistics from May 2023 to May 2024 (Fig. 2), the
140 region exhibits four distinct seasons, including pronounced cold and warm periods
141 (corresponding to freeze-thaw and wet-dry periods, respectively) and significant
142 diurnal temperature variations. Sub-zero temperatures occur from November to April
143 each year, with the minimum temperature reaching as low as -23°C, classifying it as a
144 typical seasonally frozen ground region. Extreme climatic effects constitute one of the
145 critical factors leading to frequent geological hazards, such as landslides in this area.
146 Field observations indicate that WD and FT actions have caused visible damage to loess
147 slopes in the study area, posing potential threats to human lives and public property

safety (Fig. 3).

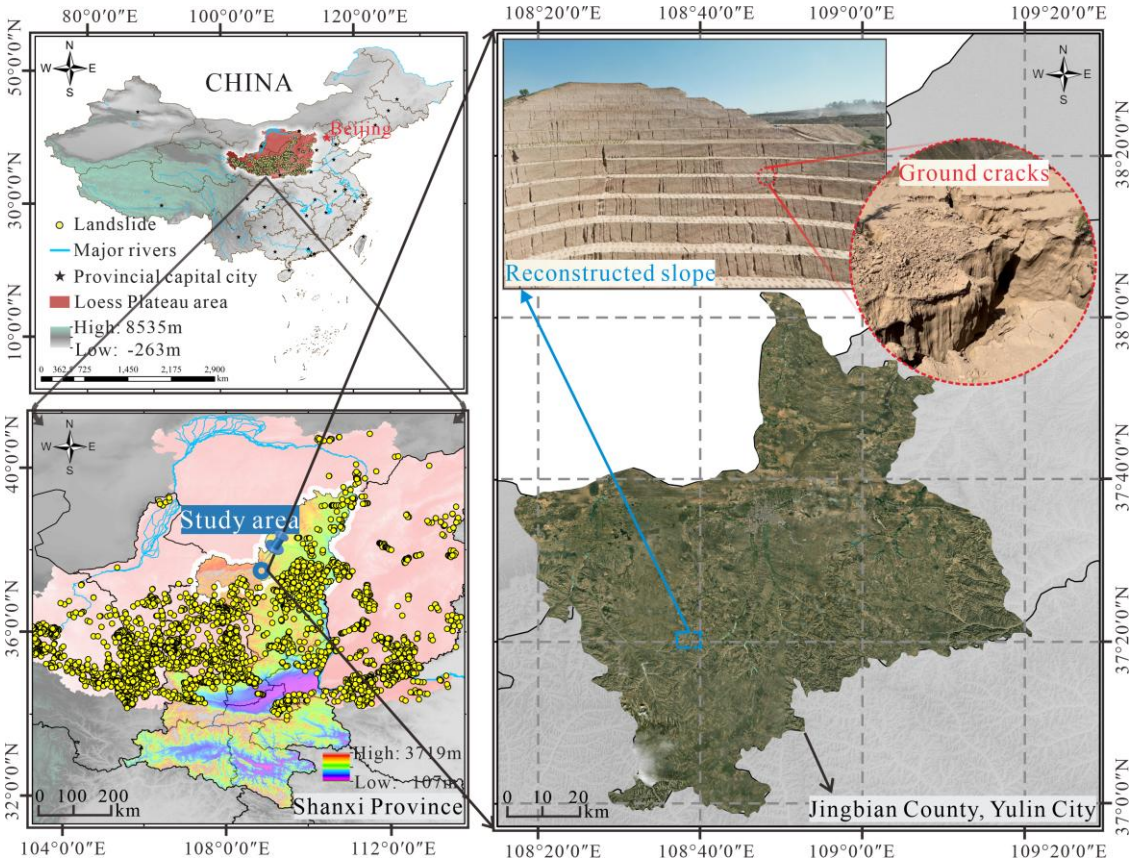


Fig. 1. Diagram of the study area.

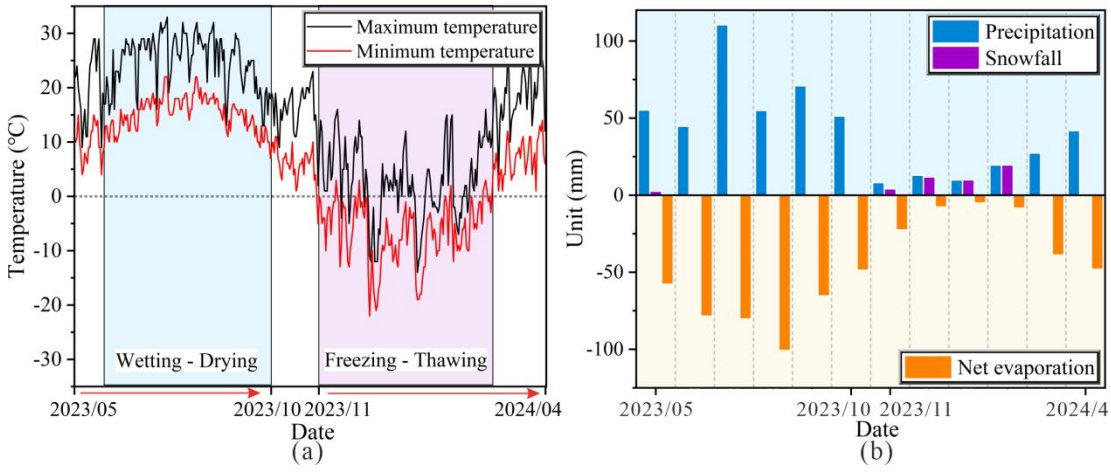


Fig. 2. Meteorological data of study area.

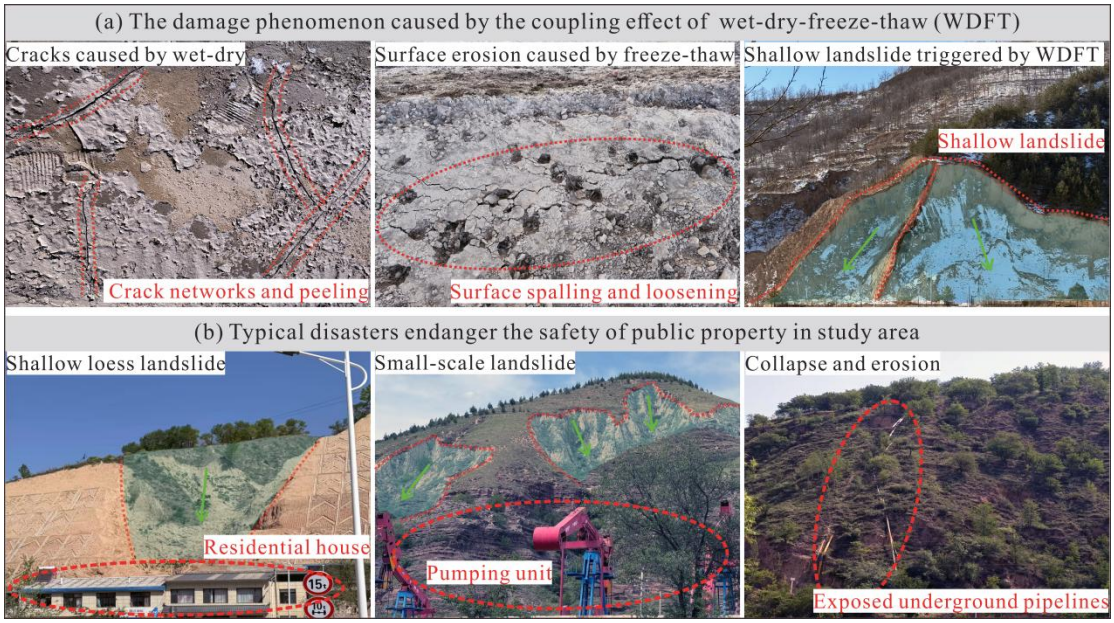


Fig. 3. Typical disasters endanger the safety of public property in study area.

2.2. Soil properties and sample preparation

The loess samples were collected from a depth of 3 meters below the surface of a loess slope within the study area. According to the Standard of Geotechnical Test Method (GB/T 50123-2019), the basic physical indexes of loess were determined and are shown in Table 1. The results indicate that the natural water content, dry density, plastic limit, and liquid limit of the loess in the study area are 5.21%, 1.67 g/cm^3, 16.8%, and 25.9%, respectively. The particle size distribution of the loess sample was determined using laser diffraction analysis (Fig. 4a). The particle size distribution curve shows that the proportions of clay (particle size < 5 μm), silt (particle size between 5-75 μm), and sand (particle size > 75 μm) in the loess sample are 4.8%, 83.3%, and 11.9%, respectively. According to the Standard of Geotechnical Test Method (GB/T 50123-2019), the loess was uniformly prepared into cylindrical specimens with a diameter of 61.8 mm and a height of 20 mm (Fig. 4b). Macroscopic and microscopic observations of the samples

revealed that the initial, untreated specimens possessed relatively smooth surfaces without significant crack development and exhibited a relatively dense structure.

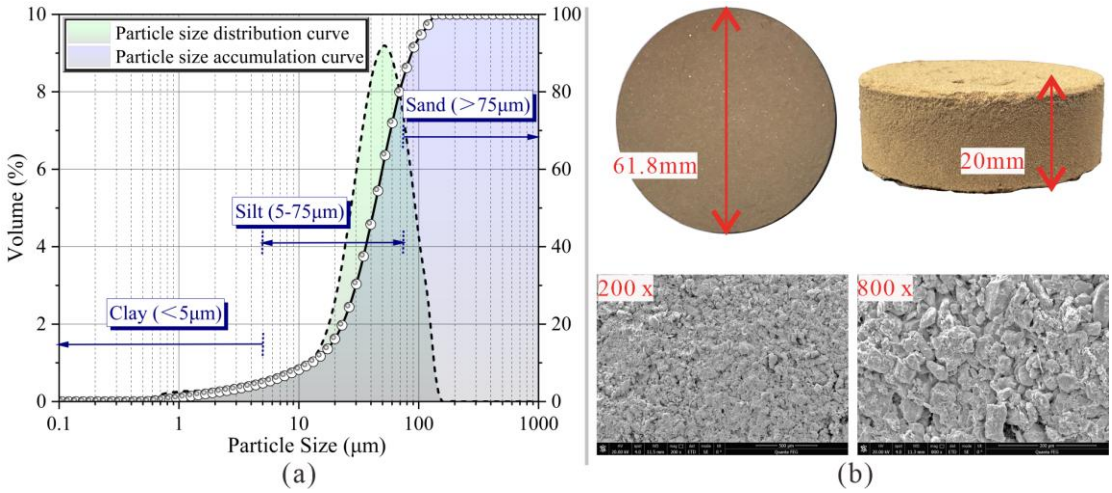


Fig. 4. (a) Grain size distribution of experimental loess and (b) Macroscopic and microscopic photos of loess samples.

Table 1 Basic physical properties of sample.

Soil type	ω (%)	ρ_d (g/cm^3)	ω_p (%)	ω_L (%)	I_p	I_L
Loess	5.21	1.67	16.8	25.9	9.1	-1.27

Notes: ω, Natural water content (%); ρ_d, Dry density (g/cm^3); ω_p, Plastic limit (%); ω_L, Liquid limit (%); I_p, Plasticity index; I_L, Liquidity index.

2.3. Methods

2.3.1. Experimental methods

To address the coupled deterioration of loess under natural environmental conditions, this study designed three cyclic modes for comparative testing: WD cycles, FT cycles, and WDFT coupling cycles. It is widely accepted among scholars that the initial cycle has a significant impact on the microstructure and physico-mechanical properties of soils, which stabilize after 5-10 cycles[39]. Based on previous research, each cyclic mode was set to 10 cycles. Considering the nonlinear deterioration of loess with

increasing cycles and to minimize the number of specimens, a method of progressively increasing intervals was adopted. Key measurement points were set at 0 (initial sample), 1, 3, 5, 7, and 10 cycles (Fig. 5a)[12]. As shown in Fig. 5b, in this study, the moisture content of WD cycle was controlled between the wetting treatment (20% moisture content) and the drying treatment (5% moisture content). Due to extreme precipitation and other factors, the loess is at a high moisture content. Therefore, 20% moisture content has been set as the target moisture content following wetting. The lower limit of the moisture content in the test was approximately 5%, which is quite similar to the natural moisture content of 5.21%. The WD cycle procedure involved placing the specimen on an electronic balance and uniformly adding distilled water dropwise onto its surface using a dropper with a rubber bulb until the target water content (20%) was reached. After wetting all specimens, they were wrapped in plastic film for 24 hours of sealed curing to ensure sufficient moisture migration. The samples were put into an electric blast drying oven and dried at 60 ℃ until 5% moisture content to simulate natural air-drying conditions [6]. First, preliminary experiments were conducted to determine the duration of freezing (24h) that would result in the complete freezing of the samples. The wetting method for the FT cycles was identical to that of the WD cycles. After the wetting treatment (20% moisture content), in order to simulate the water loss during the freeze-thaw process under natural conditions, the samples were placed in a freeze-thaw chamber at -20°C in an open environment for 24h. Then, in a 25°C environment, the moisture content was continuously measured by weighing until the moisture content of the samples dropped to 5% and the samples completely thawed,

206 with all ice crystals inside the samples completely melting. The WDFT coupling cycle
207 involves re-wetting the sample to the target moisture content (20%) after completing
208 the WD process, followed by FT treatment of the specimen, ensuring that the moisture
209 content is precisely controlled to remain consistent in each cycle, thereby constituting
210 a complete WDFT cycle.

211 *2.3.2. Physical property tests*

212 To investigate the degradation effects of different cyclic modes and cycle numbers on
213 the physical properties of loess, tests were conducted for P-wave velocity, thermal
214 conductivity, electrical resistivity, and SEM (Fig. 5c). P-wave velocity, thermal
215 conductivity and electrical resistivity tests, performed via non-destructive methods,
216 reflect soil compactness, internal structural defects, and cracks development. SEM
217 allows for the direct visualization and quantification of changes in the soil
218 microstructure. P-wave velocity was tested using an RSM-SY6 nonmetallic ultrasonic
219 detection analyzer with a transmitting channel and two receiving channels, a main
220 frequency of 600 MHz, a scanning speed of more than 20 cycles/second, high sensitivity,
221 a penetration distance. In this paper, the transient plane heat source method (TPS) was
222 used to measure the thermal conductivity of the samples, offering high measurement
223 accuracy with an error within 5% [41]. The electrical resistivity was measured using a
224 TH2811D LCR digital bridge. With the test signal frequency ranging from 50 Hz to 200
225 kHz and under constant current conditions, the two-electrode method was employed to
226 directly measure the voltage drop across the specimen. The resistivity of the loess
227 sample was then calculated from this voltage drop, as shown in Eq. (1).

$$\rho = \frac{\Delta V}{I} \cdot \frac{S}{L} = R\frac{S}{L} \quad (1)$$

where ρ is the electrical resistivity ($\Omega \cdot m$), R is the electrical resistance (Ω), ΔV is the voltage difference (V), I is the intensity of current passing through the soil sample (A), L is the length of the sample (m), and S is the cross-section area of the sample (m^2).

2.3.3. Direct shear test

To investigate the effects of different cyclic modes and cycle numbers on the mechanical properties of loess, direct shear tests were conducted using a TT-ADS4 automatic direct shear apparatus (Fig. 5c). The device is equipped with a high-precision vertical loading system (±0.1 % F.S. accuracy), enabling stable application of normal stress. After undergoing different cyclic treatments, direct shear tests were conducted under the final moisture content condition of loess samples (5% moisture content). The loess specimens were sheared at a constant displacement rate of 0.8 mm/min under vertical stresses of 50 kPa, 100 kPa, 200 kPa, and 300 kPa. The instrument features a data acquisition and processing system, allowing real-time monitoring and recording of the stress-displacement response during shearing. In this study, the shear strength of the specimen was defined as the peak stress observed in the stress-displacement curve prior to significant stress softening.

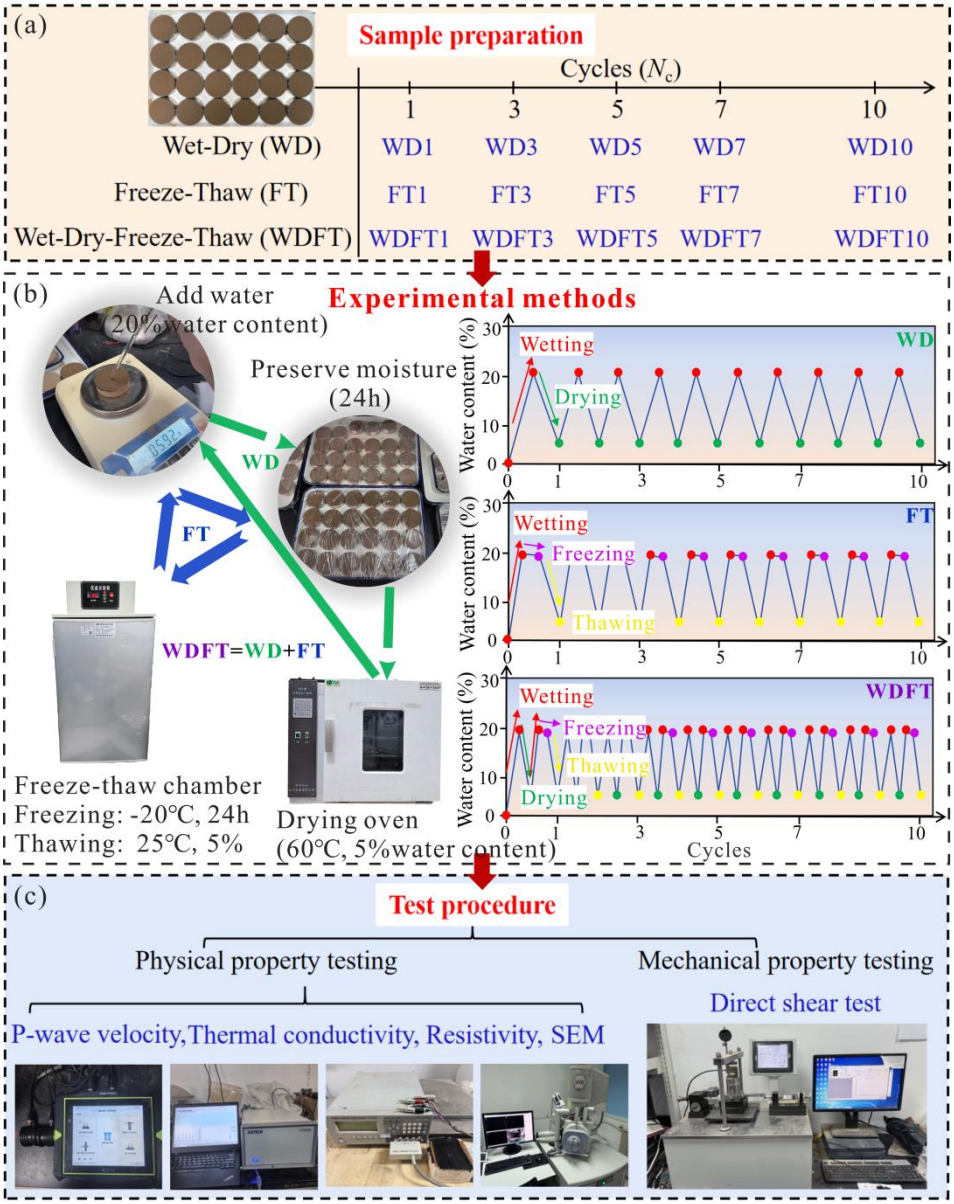


Fig. 5. Schematic diagram of research.

3. Experimental results

3.1. Variations of P-wave velocity and thermal conductivity

Fig. 6 illustrates the variation patterns of P-wave velocity and thermal conductivity under different cyclic modes. The trends for both parameters are highly consistent across the three cyclic modes, showing a progressive decline with increasing cycle numbers. Before the 5 cycles, the degrading effect of FT cycles on P-wave velocity and

thermal conductivity is slightly greater than that of WD cycles. After 5 cycles, the influence of WD cycles gradually surpassed that of FT cycles. Under the same number of cycles, the impact of WDFT coupling cycles on both P-wave velocity and thermal conductivity is significantly stronger than that of individual WD or FT cycles. After the 10th cycle, the P-wave velocity and thermal conductivity of loess specimens under WDFT coupling cycles decreased by 42% and 39%, respectively. Under WD cycles, the reductions were 37% and 36%, respectively, while under FT cycles, they were 28% and 32%, respectively. These results indicate that the structural damage inflicted by WDFT coupling cycles on loess is far greater than that caused by any individual cyclic mode. The material shows higher sensitivity and more severe degradation in response to temperature variations under the coupled action.

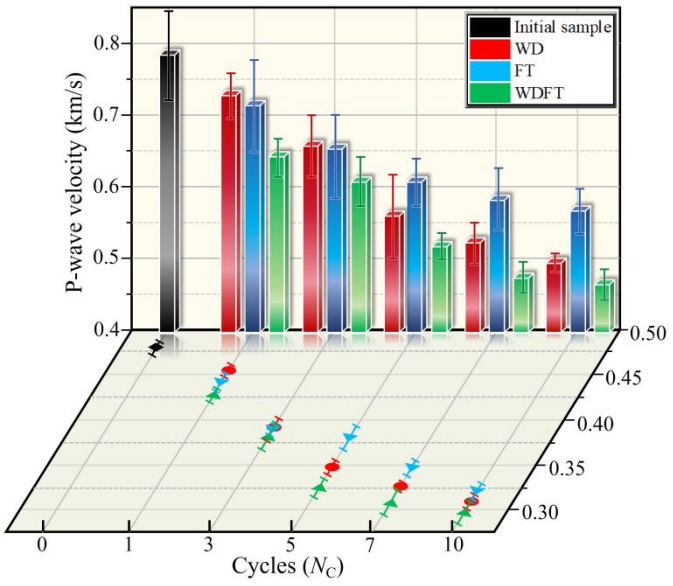


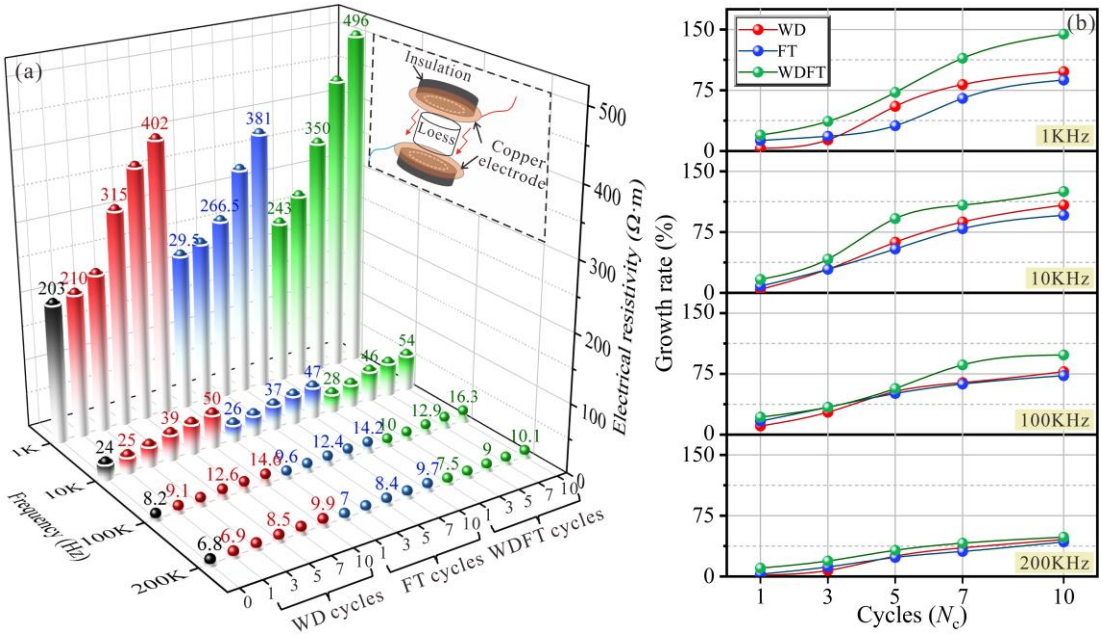
Fig. 6. Influences of different cycles on wave velocity and thermal conductivity.

3.2. Electrical resistivity change characteristics

The electrical conduction paths in soil are formed through soil particle contacts, pore water, and the combination of particles and pore water. The pore water plays a crucial

role as the key medium for ion migration in moist soil and is typically the most effective conduction path [42]. In this study, all loess specimens were in a dry state during resistivity testing after completing the cyclic treatments, meaning continuous liquid-phase conduction paths were inactive. Therefore, the changes of resistivity are attributed to variations in the internal structural characteristics of the specimens, primarily including the contact state of particles and the pore structure.

Fig. 7 presents the response patterns of loess sample resistivity under different cyclic modes and at different test frequencies. Under the same test frequency, the changes in resistivity caused by different cyclic modes show significant differences (Fig. 7a). Resistivity exhibits an increasing trend with the rising number of cycles, indicating progressive structural degradation of the specimens under cyclic actions. The increase in resistivity is most pronounced under the WDFT coupling cycles, indicating this mode induces the greatest structural alteration. The magnitude of resistivity shows a negative correlation with the test frequency. Changes in resistivity demonstrate higher sensitivity in the low-frequency range (1-10 kHz), where the increase in resistivity with cycle number is significantly greater than in the high-frequency range (100-200 kHz), differing by nearly 2-3 times (Fig. 7b). After 10 cycles, the resistivity increase for loess specimens under the WDFT coupling cycles reaches 144% at a test frequency of 1 kHz, but is only 48% at 200 kHz. Under WD cycles, the resistivity increases are 98% and 46%, respectively, while for those under FT cycles, the increases are 88% and 43%, respectively.



289

290 **Fig. 7.** Influences of different cycles on electrical resistivity.

291 *3.3. Direct shear test results*

292 *3.3.1. Stress-strain curve*

293 Fig. 8 shows the shear stress-displacement relationship curves of specimens under
294 various cyclic modes (different colors characterize the different vertical pressure). The
295 results demonstrate that loess specimens subjected to no cycles or a low number of
296 cycles exhibit pronounced strong strain-softening behavior. The shear stress initially
297 increases linearly with displacement, peaks sharply, and then drops abruptly. This brittle
298 failure process develops rapidly, making it difficult for the data acquisition system to
299 fully capture the post-peak stress decay phase. Consequently, the transition between
300 peak strength and residual strength appears nearly vertical. With increasing cycle
301 numbers, the mechanical properties of the specimens change significantly. After 10
302 cycles, the failure mode of the specimens evolves from strong strain softening to weak
303 strain softening. Under all three cyclic modes, the peak stress of the specimens shows

varying degrees of attenuation as the cycle number increases. The attenuation of peak stress is most pronounced under the WDFT coupling cycles, significantly greater than the reductions observed under individual WD or FT cycles. Furthermore, the extent of peak shear stress attenuation also exhibits some variation under different vertical pressure conditions.

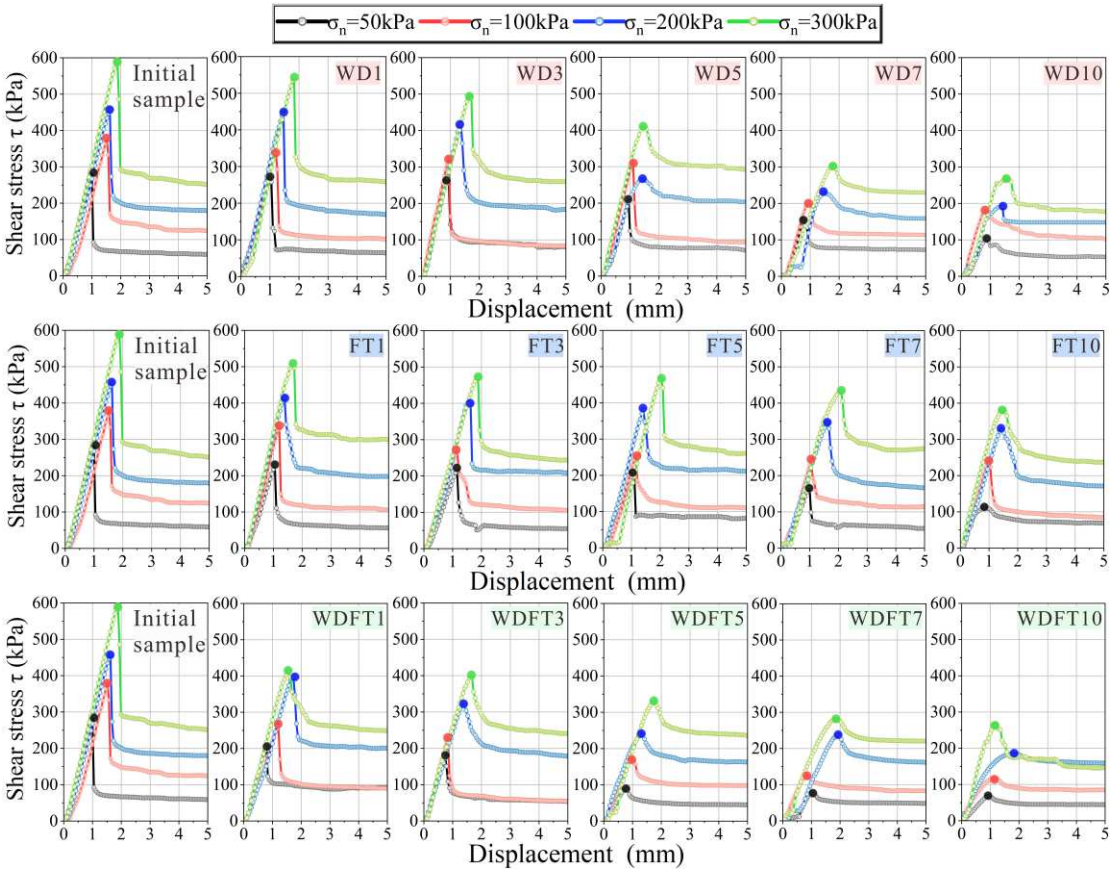


Fig. 8. Curves of shear stress versus shear displacement under WD, FT and WDFT cycles.

3.3.2. Shear strength characteristics

As shown in Fig. 8, under the four vertical stress conditions of 50 kPa, 100 kPa, 200 kPa, and 300 kPa, the shear strengths of the initial loess specimens without cyclic treatment are 287 kPa, 378 kPa, 457 kPa, and 591 kPa, respectively. To further compare the degradation effects of the three cyclic modes on specimen shear strength under these

four vertical stress conditions, this paper introduces the shear strength degradation rate as an evaluation index, as shown in Equation (2).

$$D_s = \frac{\tau^0 - \tau^n}{\tau^0} \quad (2)$$

where τ^0 is the shear strength of initial sample before cycles, τ^n is the shear strength under n number of WD, FT and WDFT cycles. With increasing cycle numbers, the shear strength exhibits varying degrees of non-linear decline under all four vertical stress conditions. The degradation rate initially increases significantly and then gradually stabilizes (Fig. 9). Due to space limitations, Table 2 only presents the fitting curve parameters and their confidence levels for the shear strength degradation rates corresponding to the three cyclic modes under the 50 kPa vertical stress condition. Under low vertical stress conditions, the shear strength degradation rate after 10 cycles is generally greater than that under high vertical stress conditions. Specifically, at 50 kPa, the final degradation rates caused by WD, FT, and WDFT cycle modes are 0.64, 0.61, and 0.76, respectively. At 300 kPa, the final degradation rates are 0.54, 0.36, and 0.56, respectively. This phenomenon may be attributed to the recompression and adjustment, to some extent, of the loosened pore structure formed by cyclic actions under high vertical pressure. Particle breakage and reorganization create an anti-degradation soil skeleton, thereby maintaining effective inter-particle contact and force chain transmission, which mitigates further damage and consequently results in a reduced magnitude of shear strength degradation. Furthermore, the degradation effects of WD and FT cycles on the shear strength of loess specimens still exhibit stage-specific characteristics. In the early cycles, the degradation from FT cycles is greater than that

from WD cycles, while in the later cycles, the degradation from WD cycles exceeds that from FT cycles.

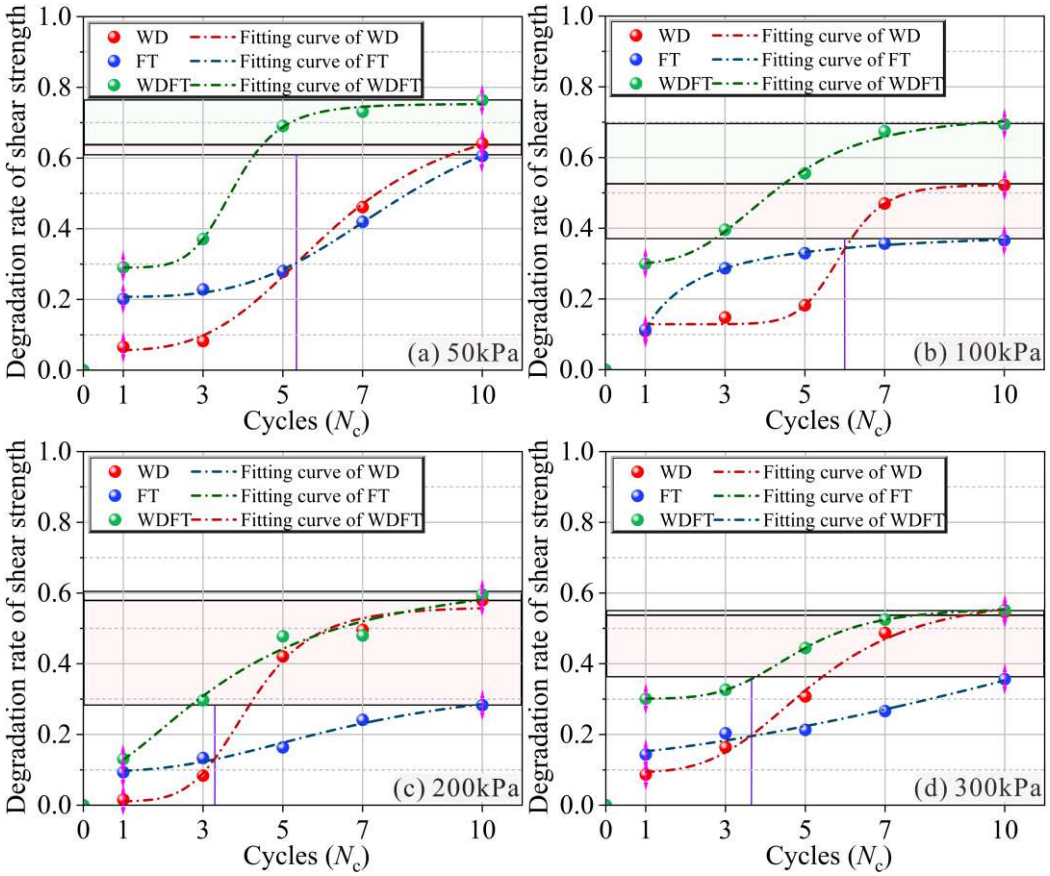


Fig. 9. Degradation rate of shear strength against different cycles under the vertical stresses of (a) 50kPa; (b) 100kPa; (c) 200kPa; and (d) 300kPa.

Table 2 The Logistic model that depicts the degradation of shear strength under the vertical stresses of 50kPa.

Cycle type	$D_s = a+b/(1+(x/c)^d)$				R^2 (Confidence coefficient)
	a	b	c	d	
WD cycle	0.74	-0.68	6.22	3.72	0.997
FT cycle	0.78	-0.57	8.02	3.90	0.998
WDFT cycle	0.75	-0.45	3.79	6.55	0.998

Notes: *D*, Degradation rate of shear strength; **x**, Number of cycles.

3.3.3. Shear strength parameters

As shown in Fig. 10, the shear strength parameters of the loess specimens exhibit

348 distinct variations depending on the cyclic mode. The degradation rates, reflected by
349 the right vertical axis, indicate that the influence of cyclic action on cohesion is
350 significantly greater than its effect on the internal friction angle. Both parameters
351 demonstrate a characteristic evolution of nonlinear attenuation followed by gradual
352 stabilization. Under both WD and WDFT cycles, both cohesion and the internal friction
353 angle decrease progressively with an increasing number of cycles. In contrast, under
354 the FT cycle, only cohesion changes markedly, while the degradation trend of the
355 internal friction angle remains relatively stable. This indicates that the concurrent
356 reduction of both cohesion and the internal friction angle is the primary reason for the
357 strength decline in specimens under WD and WDFT cycles. The decrease in cohesion
358 is the dominant factor leading to strength degradation under FT cycle. In terms of
359 degradation magnitude, for the same number of cycles, the WDFT cycle causes the
360 greatest degradation in both cohesion and the internal friction angle. The effect of the
361 FT cycle on cohesion is greater than that of the WD cycle. Specifically, under the
362 WDFT cycle mode, as the number of cycles increased from 1 to 10, cohesion decreased
363 from approximately 178 kPa to 32 kPa, and the internal friction angle decreased from
364 42° to 37°, representing reductions of 82% and 12%, respectively. Under the WD cycle
365 mode, cohesion decreased from approximately 226 kPa to 103 kPa, and the internal
366 friction angle decreased from approximately 43° to 39°, corresponding to reductions of
367 54% and 9%, respectively. Under the FT cycle mode, cohesion decreased from
368 approximately 202 kPa to 93 kPa, while the internal friction angle decreased marginally
369 from approximately 47° to 46°, resulting in reductions of 54% and 2%, respectively.

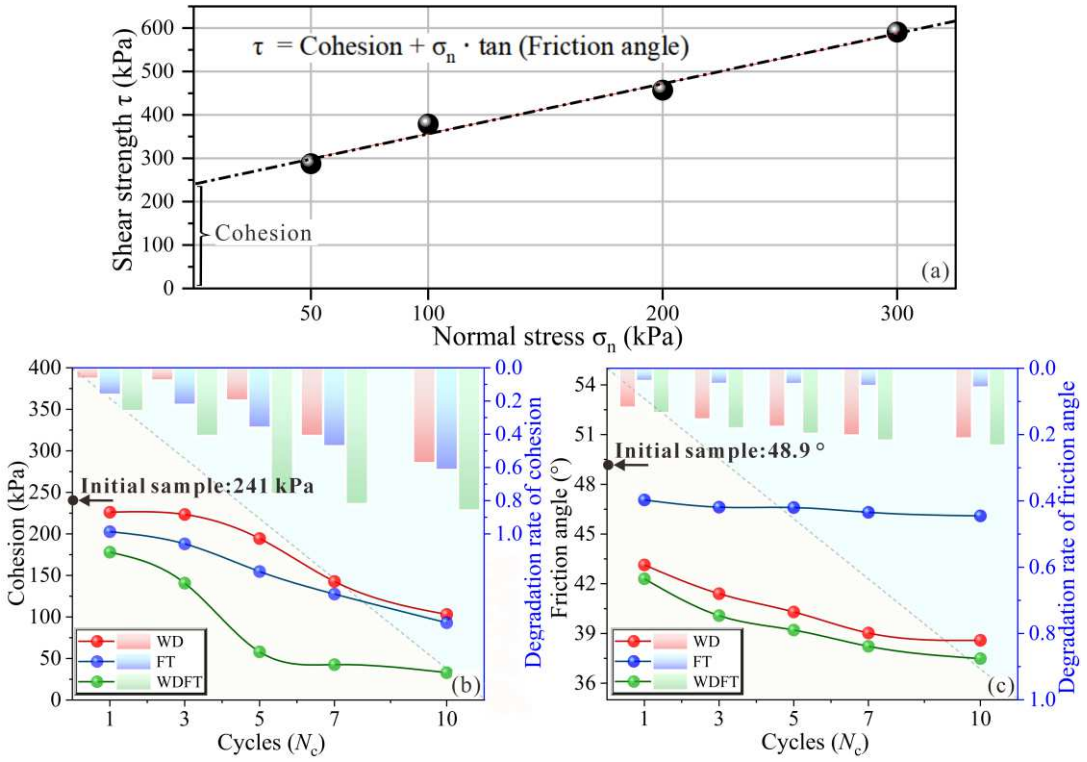


Fig. 10. Cohesion, friction angle and their degradation rates against different cycles.

3.4. Surface morphological characteristics

To analyze the apparent morphology of loess specimens after cyclic actions, Fig. 11 presents the surface failure characteristics and corresponding quantitative analysis results of crack parameters for specimens subjected to WD, FT, and WDFT cycle modes. Significant differences exist in the failure patterns induced by the different cyclic modes. In the initial stage of WD cycles, cracks primarily developed along the edges of the specimen and were mainly fine. As WD cycling progressed, existing cracks continuously extended and propagated. After 7 WD cycles, the number of micro-cracks on the specimen surface increased significantly, and these cracks interconnected to form a distinct crack network. This evolution process is closely related to the mechanism of soil under alternating WD actions. When the loess specimen is wetted, water infiltrates

383 the inter-particle spaces, leading to a thickening of the hydration films. This increases
384 the distance between particles and weakens the bonding strength. During the drying
385 phase, moisture loss makes the soil particles more prone to developing shrinkage cracks.
386 Subsequent cycles further propagate these cracks and create new crack pathways [11].
387 The impact of FT cycles on surface crack generation was relatively weak, with no
388 significant crack development observed on the surface even after 10 cycles. The
389 damage under the FT cycle mode was primarily manifested by the generation of
390 numerous pores and significant surface exfoliation (Fig. 11c). Under the WDFT cycle
391 mode, surface crack development was most pronounced. The number, width, and
392 extensibility of cracks far exceeded those observed under WD cycles. After 10 cycles,
393 the surface crack ratio (the percentage of surface crack area to the total area) reached
394 as high as 8.2%, approximately 1.4 times that observed under WD cycles (Fig. 11b).
395 Due to the coupling effect of WD and FT actions, the damage characteristics of WDFT
396 cycles were mainly characterized by a random distribution of cracks, which were
397 predominantly concentrated in vulnerable areas with pre-existing exfoliation or pores.
398 Furthermore, some cracks were difficult to heal, forming pits at their original locations
399 (Fig. 11d). As the number of cycles increased, micro-cracks continuously propagated
400 and interconnected, eventually forming large cracks that penetrated the specimen
401 surface. In addition, cracks not only appeared on the top surface of the specimen but
402 could also develop on its sides (Fig. 12). The generation and propagation of these
403 macroscopic shear cracks are also a direct cause of the overall reduction in the
404 mechanical properties of the loess. The WD and WDFT cycle modes transformed the

soil from a continuous and dense state into a layered structure, while the FT cycle mode primarily promoted the formation of a porous internal structure.

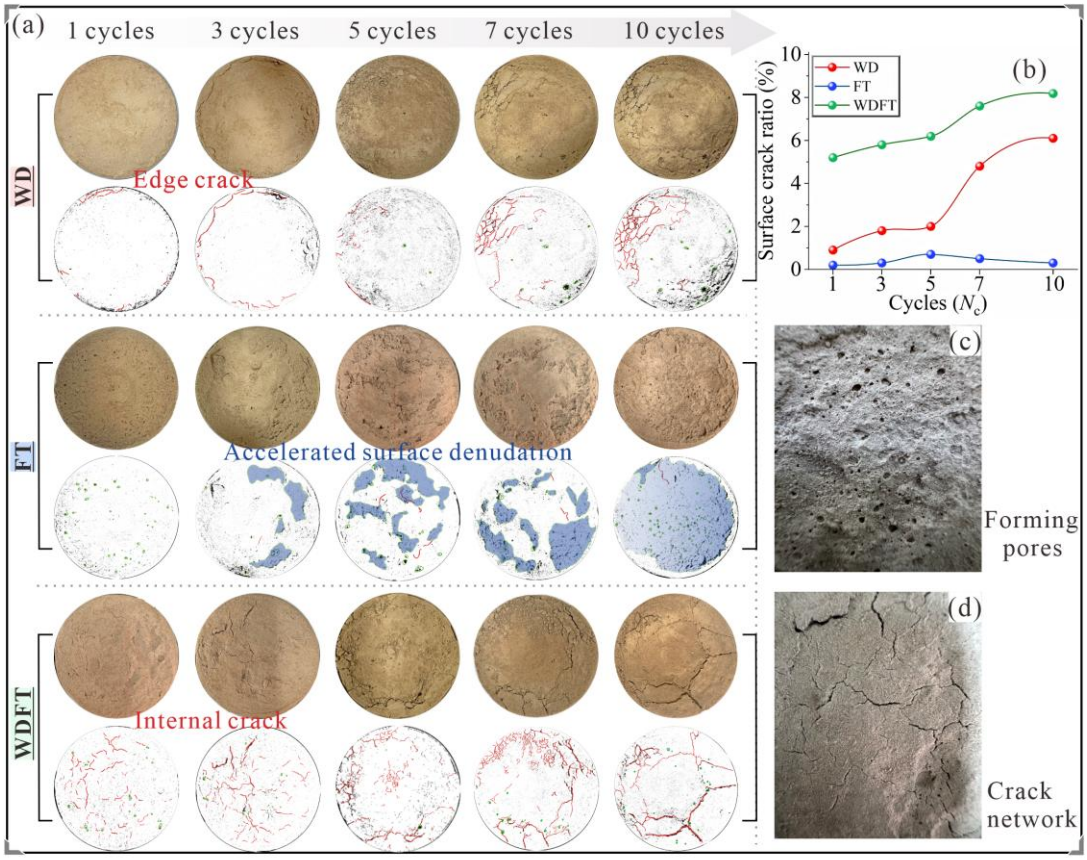


Fig. 11. Apparent morphology of loess samples under WD, FT and WDFT cycles.

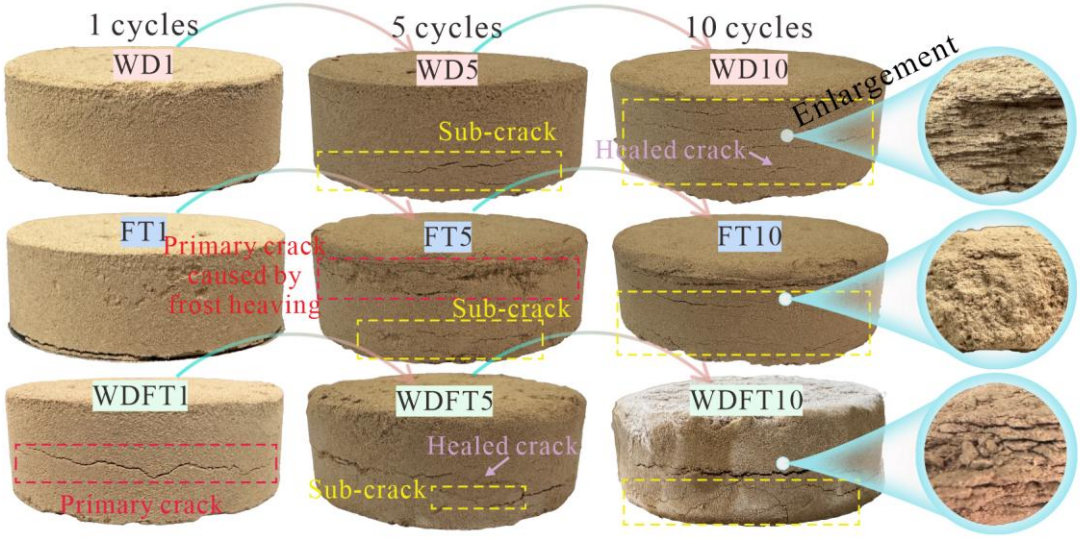


Fig. 12. Variation in the morphology of the side surface.

3.5. SEM analysis

412 *3.5.1. Microscopic morphology*

413 Fig. 13 presents SEM images of loess specimens subjected to different cyclic modes.
414 The characteristics of the pore structure are closely related to the macroscopic physical
415 and mechanical properties of the material. This study conducted a qualitative analysis
416 of the microstructural evolution of the specimens based on factors such as particle
417 morphology and distribution, particle contact patterns, and pore morphology and
418 distribution. The initial, untreated specimen exhibited a relatively intact structure with
419 regularly shaped particles arranged compactly. As the number of WD cycles increased,
420 large particles and aggregates within the loess specimen fragmented, and pores
421 interconnected to form relatively distinct, connected micro-cracks. The connection
422 mode between aggregates gradually transitioned from face-face contacts to a
423 combination of point-face and point-point contacts. Under the alternating WD actions,
424 the repeated movement and dissolution effects of moisture prompted particle
425 rearrangement, and the microstructure gradually evolved into a dispersed structure.
426 After the first FT cycle, numerous new pores appeared within the aggregates. With
427 continued FT cycling, particles from broken aggregates accumulated in localized areas,
428 exhibiting a typical stacked particle morphology. After 10 cycles, the proportion of
429 individual particles increased significantly, displaying irregular shapes. The soil
430 skeleton particles were primarily connected through a mosaic pattern combining point
431 contacts and face contacts, with the overall structure becoming looser. Structural
432 degradation under WDFT cycling was the most severe. The particle structure was
433 extremely loose, with a significant increase in the number and size of pores. Some large

particles directly exfoliated, markedly reducing structural integrity. The inter-particle structure consisted mainly of mosaic contacts and framework contacts.

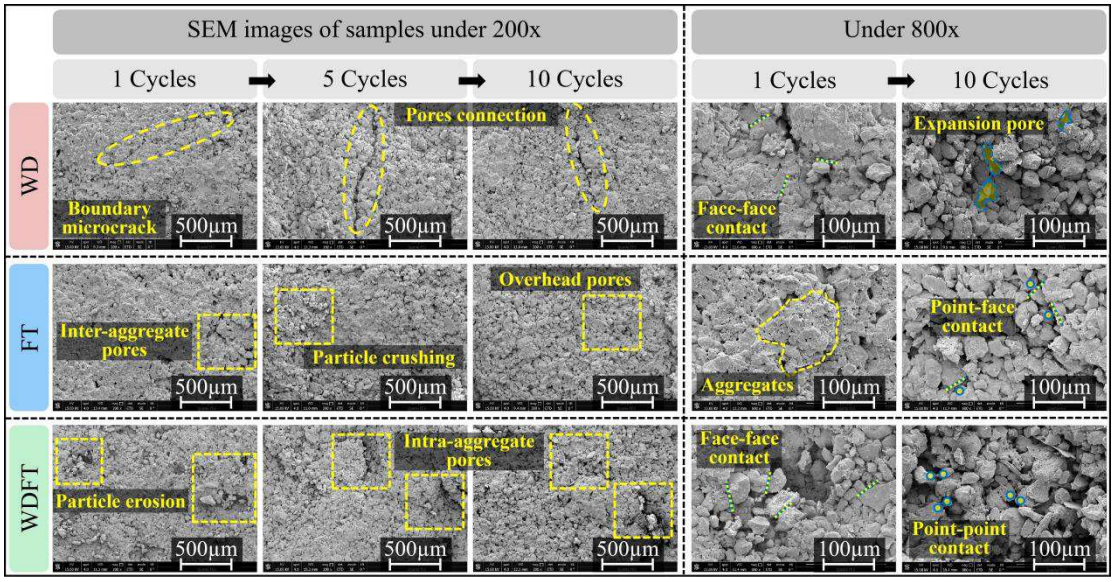


Fig. 13. Microstructural morphology of loess samples under 200x and 800x.

3.5.2. Quantitative analysis of pore structure

To accurately characterize the evolution of the specimens' microstructure after cyclic actions, this study analyzed SEM images at a magnification of 200x. Four SEM images were taken from a flat area at the center of each specimen, and the microstructural parameters were obtained as the average values from multiple images. This study used IPP (Image-Pro Plus) software to determine the threshold through multi-visual and original image comparison methods, converted grayscale images into binary images, removed truncated pores at the image edges, and performed image calibration using a scale corresponding to the image. The required parameters for analyzing the pore structure were selected, including including porosity, pore size distribution, pore angular orientation, and fractal dimension. Among them, porosity is defined as the ratio of the extracted pore area to the total area of the image. The pore diameter is the average

length of the diameters measured at 2° intervals joining two outline points, and passing through the pore's centroid. The porosity direction angle is the angle formed by the long axis of the pore and the horizontal reference plane. Fig. 14 illustrates the quantitative pore extraction process and the microstructural parameters of the initial specimen. Pores were classified based on their diameter into macropores (d > 32 μm), mesopores (8 μm < d < 32 μm), small pores (2 μm < d < 8 μm), and micropores (d < 2 μm). The fractal dimension (D_f) can characterize the complexity and irregularity of pore morphology. The fractal dimension was calculated using Eq. (3).

$$\log_n \mathrm{P} = \frac{1}{2} D_f \cdot \log_n \mathrm{A} + C \tag{3}$$

where P and A are the perimeter and area of pores, respectively, C is the fitting constant, n is the base number of logarithm, and 10 is taken in this study.

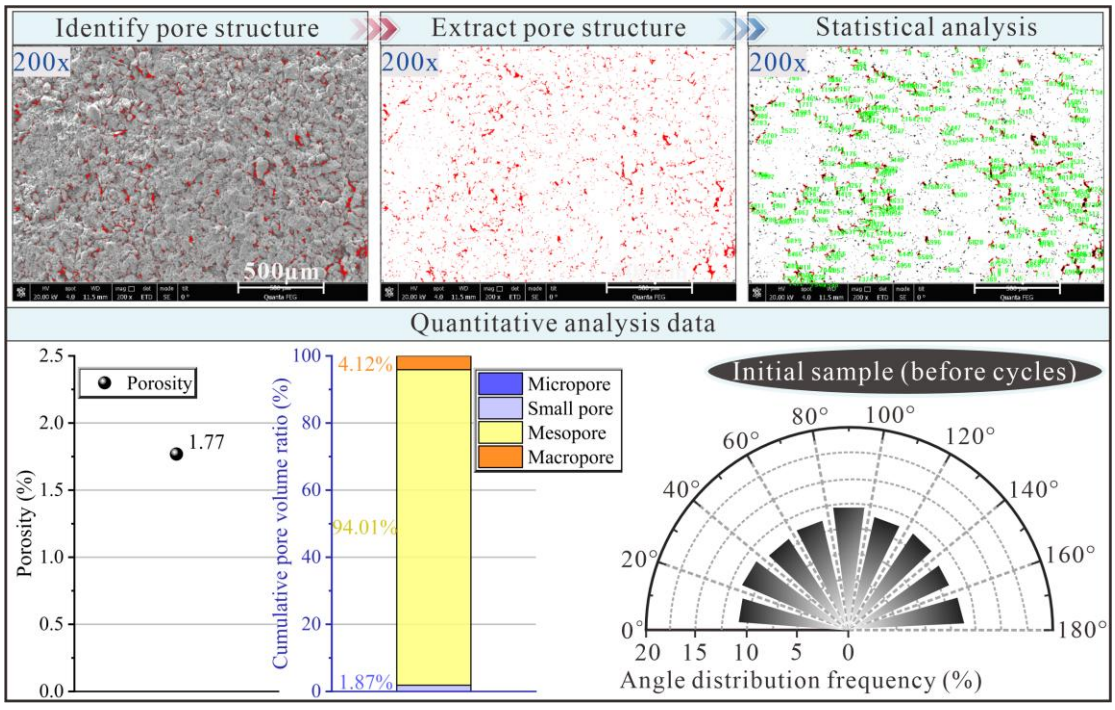


Fig. 14. Microstructural morphology quantification.

Fig. 15 illustrates the trends in specimen porosity and cumulative pore volume proportion under different cyclic modes. All three cyclic modes promoted the

development of internal pores, with porosity showing a continuous increasing trend as the number of cycles increased. After 10 cycles, the porosity of specimens under WD, FT, and WDFT cycles reached 7.83%, 7.04%, and 9.13%, respectively. Compared to the initial untreated specimen, this represents an increase of approximately 3.4%, 3.0%, and 4.2%, respectively. Regarding pore size distribution, the number of cycles had minimal impact on micropores. Therefore, changes in micropore count are not reflected in the statistics. This study primarily observed the characteristics of changes in small pores, mesopores, and macropores. The results indicate that different cyclic modes share commonalities yet possess distinct characteristics in their influence on pore size distribution. Under WD and WDFT cycles, the overall change in pore size was relatively consistent. With increasing cycle numbers, the proportion of macropores increased significantly, while the proportions of mesopores and small pores relatively decreased. Under FT cycles, as mesopores gradually transformed into macropores, a substantial number of small pores were also generated within the aggregates. Consequently, this manifested as a simultaneous increase in the number of small pores and macropores, with a relative decrease in the proportion of mesopores. After 10 cycles, the proportions of small pores, mesopores, and macropores under WD cycles were 1.3%, 87.6%, and 11.1%, respectively. The corresponding proportions under FT cycles were 7.5%, 82.5%, and 10.0%. Under WDFT cycles, they were 1.2%, 84.2%, and 14.6%, respectively. The WDFT coupling cycles had the most pronounced impact on the pore structure, not only showing the largest increase in porosity but also the highest proportion of macropores, demonstrating a synergistic promoting effect of WD and FT

cycles in facilitating pore development.

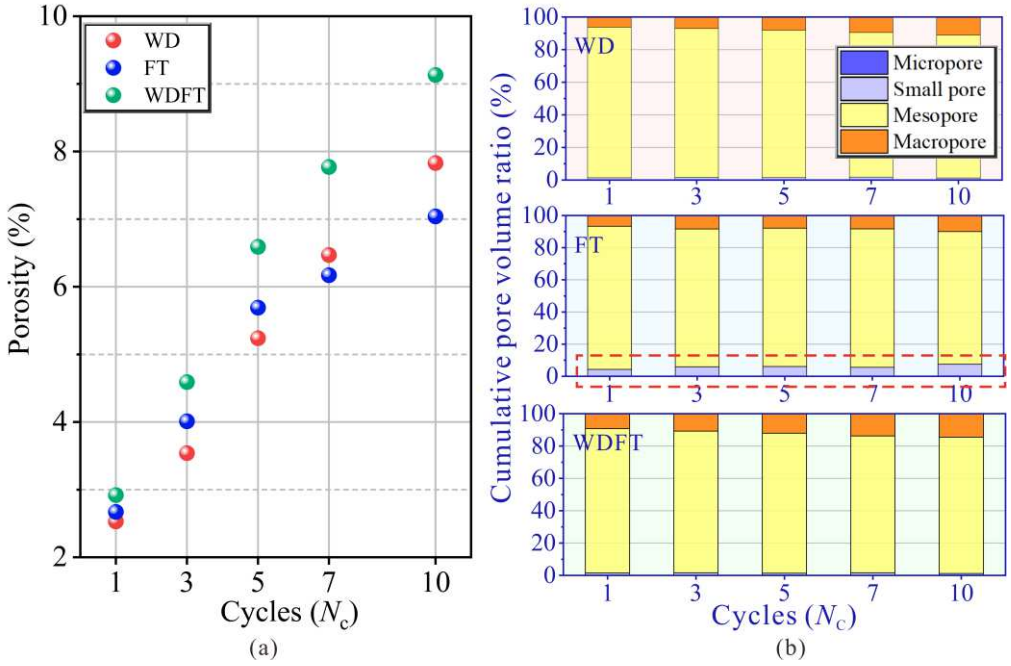


Fig. 15. Porosity and cumulative pore volume ratio of samples after each process of cycles.

To reveal the spatial distribution patterns of pores and quantify the evolution of their orientation characteristics, this study conducted statistical analysis based on pore orientation angles. The pore orientation angle is defined as the angle between the long axis of a pore outline and the vertical axis. The angle range is fixed from 0° to 180° and divided into 9 directional intervals at 20° increments. The distribution frequency of pore orientation angles within each interval was then calculated for each specimen (Fig. 16). As shown in Fig. 14, the initial specimen exhibited a relatively uniform distribution of pore angles, indicating a structure with good isotropy. After being subjected to different cyclic modes, the pore orientation of the specimens changed significantly, gradually transitioning from an initially uniform multi-directional distribution to a concentrated distribution along specific directions. The cycles significantly increased pore sizes, and the contribution of larger pores to the overall directional distribution became more

prominent, thereby strengthening the concentration trend in specific orientations. After WD cycles, the pore orientations of the specimens became significantly concentrated in the 0°-20° and 160°-180° intervals, while the distribution frequencies in other directions generally decreased. The FT cycles caused pores to develop primarily along the 60°-120° directional interval. This phenomenon may be related to the mechanism of ice crystal growth and propagation along the path of least resistance during the freezing process. Under the coupled WDFT cycles, the directional distribution of pores exhibited characteristics of both WD and FT types, showing concentration in intervals both parallel and perpendicular to the vertical axis.

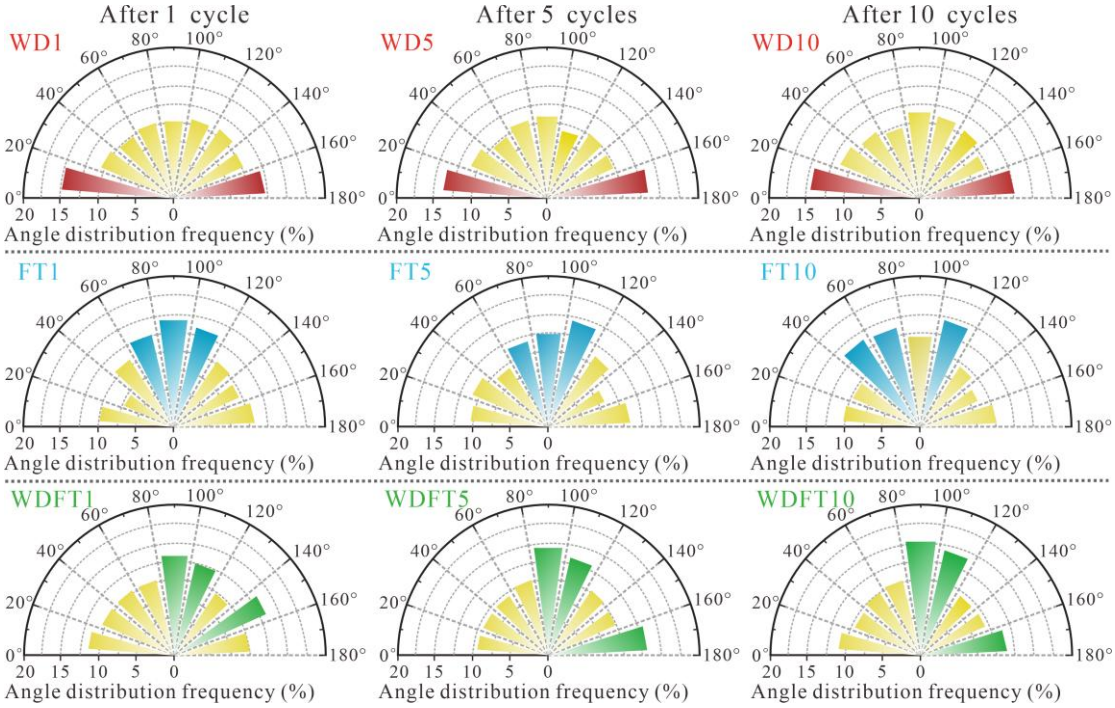


Fig. 16. The pore directional distribution.

Fig. 17a illustrates the variations in fractal dimension under different cyclic modes. The initial specimen contained approximately 150 pores exhibiting fractal characteristics. As the number of cycles increased, the number of pores with fractal characteristics continued to rise, and the curve characterizing structural complexity

shifted overall toward the upper right. Based on the evolution characteristics of the fractal dimension, the fractal dimension curve can be divided into a slow growth stage and a rapid growth stage. During the rapid growth stage, the fractal dimension increased significantly, indicating that as the number of pores increased, the irregular pore morphologies also became notably more prevalent, forming a complex and disordered pore structure. Further analysis calculated the change in the average fractal dimension of the pore structure (Fig. 17b). The average fractal dimension of pores in specimens subjected to WDFT cycles ranged from 1.176 to 1.198, which was significantly higher than that under individual cyclic actions at the same cycle number. This reflects the further complexity of microstructure evolution induced by the coupled WD and FT effects.

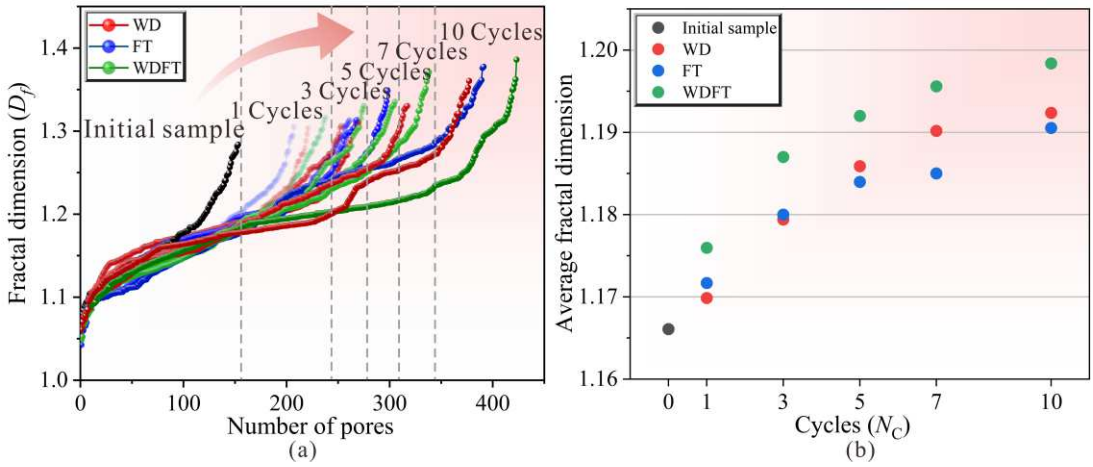


Fig. 17. Pore fractal dimension of samples after each process of cycles.

4.Discussion

4.1. Correlation analysis

This study systematically analyzed loess specimens subjected to WD, FT, and WDFT cycles, revealing the degradation patterns of the specimens from the perspectives of

macroscopic physical-mechanical properties and microstructure. The results indicate that all three cyclic modes lead to varying degrees of performance degradation in the specimens. Specifically, porosity, fractal dimension, and electrical resistivity exhibit a positive correlation with the number of cycles, while P-wave velocity, thermal conductivity, shear strength, cohesion, and internal friction angle show a negative correlation with increasing cycle numbers (Fig. 18). Both WD and FT cycles affect the physical-mechanical properties of loess by damaging its internal structure, and their damage effects are cumulative and irreversible [10]. Due to their distinct core mechanisms, their damage patterns and severity differ significantly.

The WD cycles are primarily driven by the periodic increase and decrease of moisture, causing uneven expansion and contraction of the soil mass, which in turn initiates and propagates micro-cracks [15]. The WD damage manifests as the formation of crack networks and a loose, layered structure. The WD cycles may also involve chemical effects, such as the dissolution of soluble cementing minerals in aqueous environments [25]. In contrast, the FT cycles are dominated by severe physical disruption caused by water-ice phase changes. The frost heave pressure generated by ice crystal growth during freezing promotes pore expansion and particle exfoliation [19]. During the subsequent thawing phase, as temperatures rise, moisture migration further disrupts the soil structure, continuously forming an open, porous framework. Consequently, macroscopic FT damage is characterized by numerous pores and localized exfoliation (Fig. 11c). Although both ultimately lead to the progressive degradation of physical-mechanical properties, the degree of deterioration exhibits

certain stage-specific characteristics. In the early stages of cycling, the intense phase change associated with FT cycles causes more severe structural damage to the loess, resulting in greater degradation than WD cycles. However, as the number of cycles increases, the continuous softening and cumulative damage effect of WD cycles on the soil structure become significantly more pronounced. Therefore, the detrimental effect of WD cycles gradually surpasses that of FT cycles. Under the same number of cycles, the WDFT coupling cycles had the most significant impact on all parameters. By comparing the magnitudes of change, it is evident that the damage to loess from the coupled WD and FT effects is not merely an additive combination of their individual effects but represents a more complex, nonlinearly accelerating deterioration.

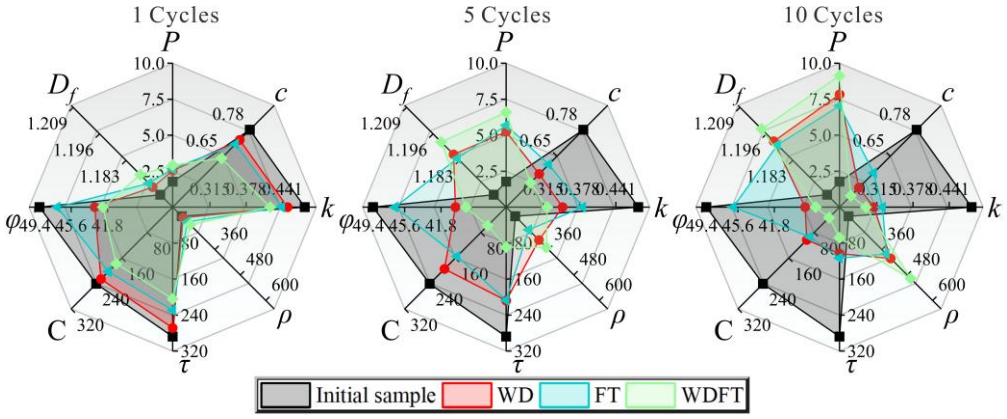


Fig. 18. Changes in micro and macro parameters. **Notes:** ***P***, Porosity (%); ***c***, P-wave velocity (km/s); ***k***, Thermal conductivity (W/m·k); ***ρ***, Electrical resistivity (Ω·m); ***τ***, Shear strength under σ_n=50kPa (kPa); **C**, Cohesion (kPa); ***φ***, Friction angle (°); $\boldsymbol{D_f}$, Average fractal dimension of pore.

To further investigate the intrinsic relationships among various parameters during the cyclic processes, this study employed Pearson correlation analysis, with the results presented in Fig. 19. In the figure, red indicates positive correlations, blue indicates negative correlations, and the absolute value of the numbers reflects the strength of the

correlation. The analysis shows that with increasing cycle numbers, the parameters exhibited strong correlations with each other. Since FT action had a minor influence on the internal friction angle, its correlation with other indicators was relatively weak. The microstructural parameters demonstrated high correlations with all physical-mechanical parameters, reaching a significance level at 0.001. In summary, this study confirms that the evolution of the microstructure is the fundamental mechanism driving changes in the macroscopic physical-mechanical properties of loess. Physical indicators such as wave velocity, thermal conductivity, and electrical resistivity, along with mechanical indicators such as shear strength and cohesion, can all serve as effective parameters for evaluating the degree of structural damage in the specimens.

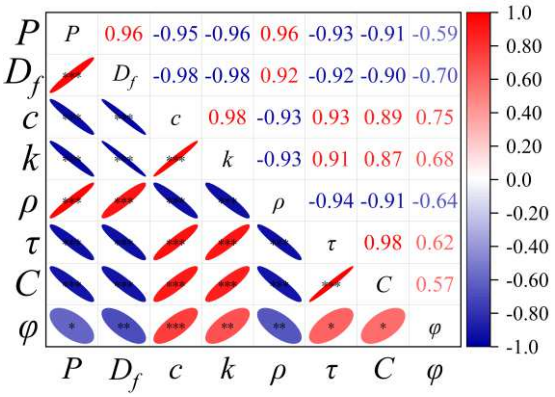


Fig. 19. Pearson's correlation matrix for parameters. **Notes:** *, ** and *** denote that parameters are significant at the 0.05, 0.01 and 0.001 level.

4.2. The influence mechanism of WDFT cycles

Loess materials are subjected to alternating wetting during the rainy season and drying during the arid season, while also experiencing freezing due to sharp temperature drops in winter and thawing caused by rising temperatures in spring. This complex natural environmental condition indicates that the gradual deterioration of loess material

properties results not from a single WD or FT action, but from the synergy and superposition of multiple processes under coupled WDFT effects [45]. This study focuses on investigating the damage evolution mechanism of loess under coupled WDFT action (Fig. 20).

In the subsequent drying stage, water evaporation releases pore water pressure, causing anisotropic and uneven shrinkage of the soil. When the shrinkage stress between internal particles exceeds the tensile strength, corresponding desiccation shrinkage micro-cracks are generated. Although some dissolved substances may re-precipitate, creating secondary cementation, its bonding strength is far lower than that of the primary cement, making it ineffective in restoring the integrity of the initial structure. During the second wetting stage, some of the interconnected cracks formed by the previous WD action become new preferential pathways for moisture migration, significantly enhancing water infiltration capacity. Some cementing minerals further decompose under hydration, causing the splitting and disintegration of some aggregates and increasing the distance between particles, which creates favorable conditions for subsequent freeze-thaw damage. In the freezing stage, the volume expansion resulting from the phase change of pore water exerts significant crystallization pressure on the surrounding mineral particles. The formation of ice lenses not only promotes the propagation of existing cracks but also generates new micro-cracks within some particles. In the subsequent thawing stage, the fragmented particles rearrange under gravity, and the original pore structure cannot be restored, resulting in an overall loosening of the soil structure.

As the number of cycles increases, the crack development induced by WD action and the structural fragmentation caused by FT action mutually reinforce each other, establishing a positive feedback amplification mechanism. The crack network provides pathways for moisture migration and the development of ice lenses, while frost heave action further enlarges the crack scale and continuously generates new pore structures. This persistently enhances the infiltration capacity of aqueous solutions and intensifies hydration processes. This coupled synergistic effect ultimately leads to the evolution of soil damage from microscopic structural deterioration to large-scale macroscopic failure. This coupled damage mechanism also provides a clearer explanation for why, under the same number of cycles, the damage extent induced by coupled WDFT action far exceeds that caused by any individual action, and why the overall damage is not simply an additive superposition of the two individual damaging effects.

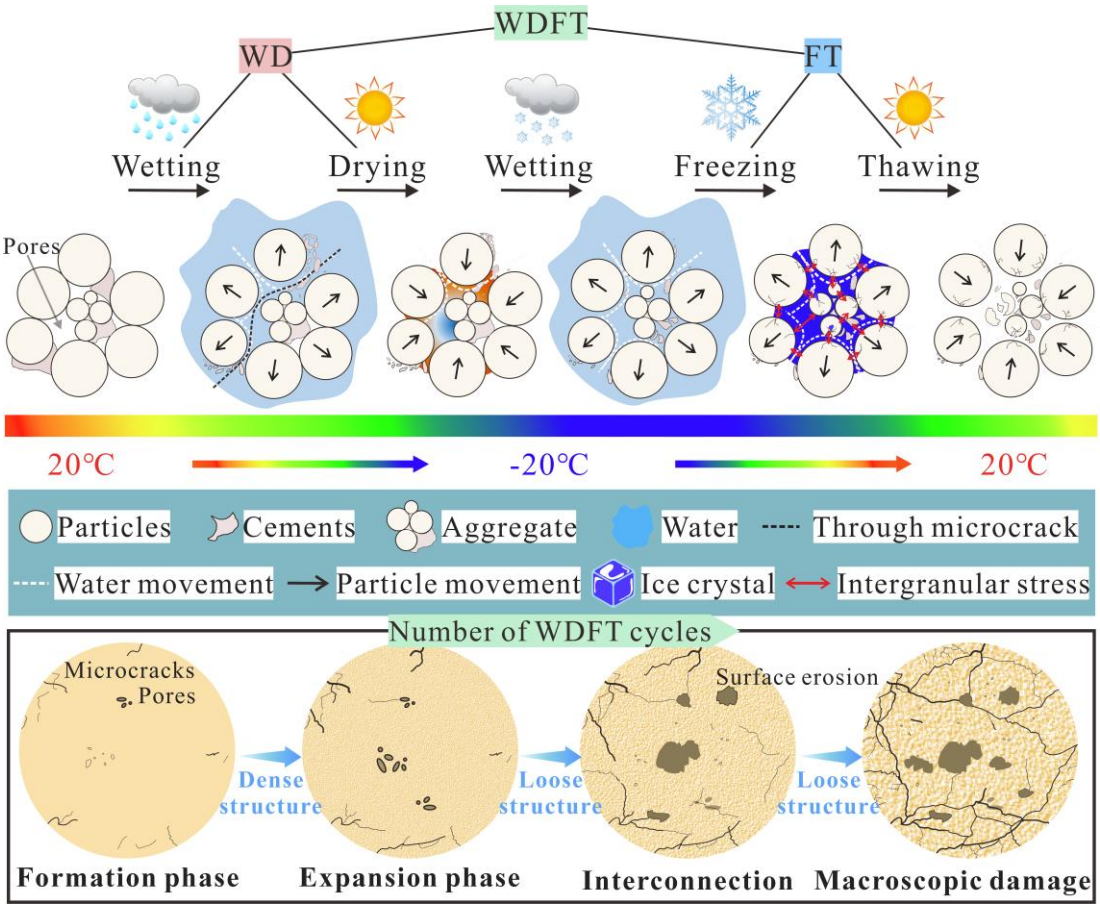


Fig. 20. The internal and macroscopic structure evolution diagram of loess during WDFT cycles.

4.3. Mechanism of loess landslide induced by extreme environmental factors

The instability and failure of loess slopes often result from a phased and progressive evolution under the long-term coupled effects of multiple environmental factors. Based on comprehensive field investigations and laboratory experimental analyses, the evolutionary mechanism of loess landslides under coupled WDFT action can be divided into the following four stages (Fig. 21).

(I) Rainfall wetting stage: Precipitation not only scours the slope surface, forming gullies, but also infiltrates into the interior of the slope along the vertical joints of the loess. Under the influence of rainwater infiltration, existing cracks further

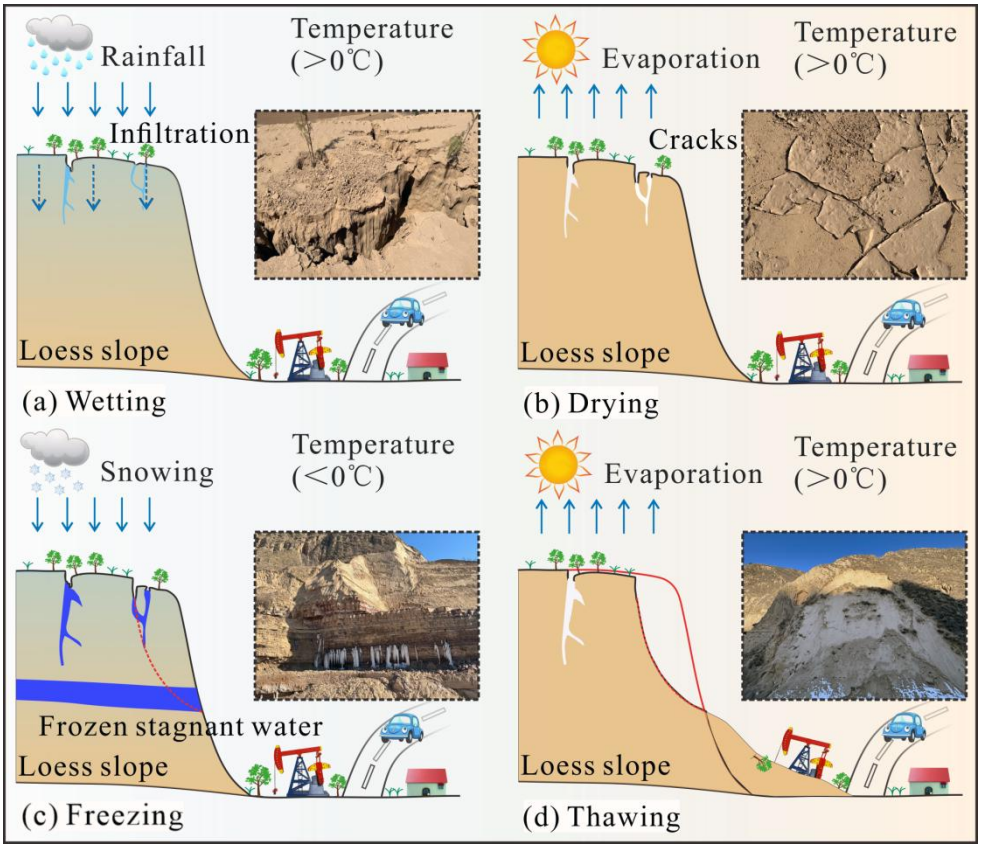
propagate, manifested by the development of surface collapse pits and the formation of preferential seepage pathways at greater depths. Due to differences in the permeability of soil layers at various depths, a potential stagnant water zone forms where infiltration is slower at specific depths. Sustained infiltration exacerbates particle migration and the stagnant water effect. Concurrently, hydration weakens the cementation strength of the soil, leading to its uneven softening and the formation of structurally weak zones within the slope.

(II) Dry and evaporation stage: Water evaporation induces overall drying shrinkage of the soil mass. When the resulting shrinkage stress exceeds the soil's tensile strength, new shrinkage cracks form near the weak zones generated by prior hydration. These cracks interconnect with the existing seepage pathways, significantly enhancing moisture migration capacity and creating favorable conditions for subsequent FT damage.

(III) Freezing stage: Under low-temperature conditions, water that has infiltrated along the cracks undergoes phase transition, forming ice lenses. This process generates significant frost heave pressure acting on the crack walls, substantially expanding the existing cracks. As drainage channels near the slope surface become blocked by ice formation, a frozen stagnant water layer develops within the slope mass. The soil in this layer suffers from the dual effects of hydration-induced softening and frost heave damage, becoming a key weak zone governing slope stability. The potential shear outlet formed during this stage, together with the continuously propagating frost heave cracks, constitutes a complete potential sliding surface.

(IV) Thawing stage: As temperatures rise, the ice melts, and water is discharged intensively along the drainage channels on the slope surface. The resulting seepage pressure and internal erosion significantly reduce the shear strength of the potential sliding surface. Once the stress state of the slope exceeds its critical bearing capacity, overall sliding failure occurs [27].

It is important to emphasize that the sliding failure of a loess slope may occur after a single or several cycles of coupled WDFT action, or it may manifest during a specific WD or FT phase within a WDFT coupling cycle. Therefore, slope sliding cannot be attributed to any single process, but is instead the inevitable outcome of the coupling and cumulative damage of multiple physical and chemical processes, including water infiltration, particle migration, crack propagation, hydration softening, and frost heave fracturing [3, 46]. This multi-process coupled, progressive failure mechanism can provide a theoretical basis for the stability assessment and hazard prevention of loess slopes in regions with significant seasonal climatic variations.



675

676 **Fig. 21.** Mechanism of loess landslides induced by WDFT cycles.

677 **5.Conclusion**

678 This study focuses on loess regions subjected to seasonal wet-dry (WD) and freeze-
679 thaw (FT) cycles. By employing multiple technical methods, including P-wave velocity
680 testing, electrical resistivity measurement, scanning electron microscopy (SEM)
681 analysis, and direct shear tests, it systematically reveals the evolution of the
682 microstructure and the degradation patterns of macroscopic physical and mechanical
683 properties of loess materials under WD cycles, FT cycles, and wet-dry-freeze-thaw
684 (WDFT) cycles. The research aims to investigate the damage inflicted on loess
685 materials by coupled WDFT action in extreme environments and the disaster-causing
686 mechanisms of landslides thereby induced. The results of this paper can be summarized

as follows:

(1) Under the three cyclic modes, both the P-wave velocity and thermal conductivity of the loess specimens exhibited a phase-wise decrease with increasing cycle numbers, characterized by an initial rapid decline followed by gradual stabilization. Changes in the pore structure hindered efficient electrical conduction through the soil skeleton, leading to an increasing trend in electrical resistivity. The variation in electrical resistivity showed clear frequency dependence, with the low-frequency range (1-10 kHz) being more sensitive to structural damage in the soil. The deterioration effect of the WDFT coupling cycles on physical properties was significantly more pronounced than that of individual WD or FT cycles. After 10 cycles, the reductions in P-wave velocity and thermal conductivity reached 42% and 39%, respectively, while the electrical resistivity increased by 144% at a test frequency of 1 kHz.

(2) The evolution of the mechanical behavior of loess exhibits clear dependence on the cyclic mode. The stress-strain curve of untreated specimens displays strong strain-softening behavior, which transitions to weak strain softening with an increasing number of cycles. Both shear strength and strength parameters show a nonlinear decrease as the cycle numbers rise, with the degradation rate increasing rapidly in the initial stage and tending to stabilize later. WD and WDFT coupling cycles lead to the simultaneous degradation of cohesion and the internal friction angle, whereas FT cycles primarily cause a reduction in cohesion.

(3) Qualitative and quantitative analyses of both macroscopic morphological

features and microstructural changes jointly reveal the evolutionary patterns of the soil structure. WD cycles primarily form a directionally developed crack network, while FT cycles mainly lead to the generation of a porous structure. The WDFT coupling cycles exhibit the destructive characteristics of both, forming a more significant interconnected damage system. With an increasing number of cycles, the porosity of the specimens continuously increases, and the directionality as well as the complexity of the pores are enhanced. While cyclic actions lead to an increase in the proportion of macropores, FT cycles also result in a rise in the proportion of small pores.

(4) The degradation effects of different cyclic actions exhibit significant temporal variation and stage-specific characteristics. In the early stages of cycling, FT has a greater impact on specimen performance than WD. As the number of cycles increases, the cumulative damage effect of WD cycles gradually becomes dominant. The crack networks formed by WD action and the frost-induced fragmentation caused by FT action mutually reinforce each other through a positive feedback mechanism. The combined damage effect of WD and FT actions results in the most pronounced deterioration under WDFT coupling cycles, with the extent of damage far exceeding a simple superposition of individual cyclic modes. This coupled synergistic effect ultimately drives a progressive evolution of soil failure, from microstructural damage to macroscopic slope instability.

Declaration of competing interest

The authors declare that they have no known competing financial interests or personal

relationships that could have appeared to influence the work reported in this paper.

Acknowledgments

This research was supported by the National Key Research and Development Project (No.2023YFC3008401), and Open Fund of the National Key Laboratory of Loess Science (No. SKLLQG2508). We thank editor and the two anonymous reviewers for their constructive comments on the manuscript, which significantly improved the quality of the paper.

Data availability

Data will be made available on reasonable request.

Reference

Bai R, Lai Y, Zhang M, Jiang H (2024) Investigating the thermo-hydro-mechanical behavior of loess subjected to freeze-thaw cycles. Acta Geotech 19: 6305–6318.

Cai G, Liu Q, Li K, Zhang J, Liu Y, Zhou A (2023) Volume change behavior of compacted loess under drying/wetting and freezing/thawing cycles. Eng Geol 326: 12.

Chen Q, Liu Y, Wang Y, Su L, Cheng Y (2025) Investigation of coupled thermo-hydro-mechanical processes on soil slopes in seasonally frozen regions. Cold Reg Sci Tech 229: 11.

Duan G, Song F, Wang H, Rodriguez-Dono A, Wang L, Chen J (2024) Stability analysis of unsaturated loess slopes subjected to extreme rainfall incorporating creep effects. Comput Geotech 169: 17.

Han X, Hu Z, Li H, Yin Y, Zhang B, Zhang L (2024) Study on the mechanical properties and microstructural evolution of loess under different wet-dry and freeze-thaw coupled cycling paths. Case Stud Constr Mater 21: 22.

Hu C, Yuan Y, Mei Y, Wang X, Liu Z (2020) Comprehensive strength deterioration model of compacted loess exposed to drying-wetting cycles. Bull Eng Geol Environ 79: 383–398.

Jia L, Yu K, Li Z, Li P, Zhang J, Wang A, Ma L, Xu G, Zhang X (2022) Temporal and spatial variation of rainfall erosivity in the Loess Plateau of China and its impact on sediment load. Catena 210: 14.

Jing J, Hou J, Sun W, Chen G, Ma Y, Ji G (2022) Study on Influencing Factors of Unsaturated Loess Slope Stability under Dry-Wet Cycle Conditions. J Hydrol 612: 11.

Kong F, Xu Y, Hu Z, Du H, Zhang J, Zhang Z, Hao W (2024) Disintegration characteristics of sodic-saline loessial soil after freeze-thaw and wet-dry cycles. Earth Surf Process Landf 49: 2229–2244.

Kong J, Zhuang J, Peng J, Ma P, Zhan J, Mu J, Wang J, Zhang D, Zheng J, Fu Y, Wang S, Du C (2023) Failure mechanism and movement process of three loess landslides due to freeze-thaw cycle in the Fangtai village, Yongjing County, Chinese Loess Plateau. Eng Geol 315: 18.

Lai R, Zhang Z, Zhang Y, Chen D, Shi G, Fu Q (2023) Deterioration mechanism of loess from Ili valley region of China under wet and dry cycles: evidences from shear tests. Front Earth Sci 11: 15.

Li G, Wang F, Ma W, Fortier R, Mu Y, Mao Y, Hou X (2018) Variations in strength and deformation of compacted loess exposed to wetting-drying and freeze-thaw cycles. Cold Reg Sci Tech 151: 159–167.

Li S, Wang J, Han K, Wang L, Zhang D, Dong H, Cui B (2024) Promoting effect and microscopic mechanism of train-induced vibration on loess disintegration. Eng Geol 336: 16.

Li Y, Shi W, Aydin A, Beroya-Eitner M, Gao G (2020) Loess genesis and worldwide distribution. Earth-Sci Rev 201: 22.

Lian B, Wang X, Zhan H, Wang J, Peng J, Gu T, Zhu R (2022) Creep mechanical and microstructural insights into the failure mechanism of loess landslides induced by dry-wet cycles in the Heifangtai platform, China. Eng Geol 300: 19.

Liu K, Wang X, Lian B, Hu S, Wang D, Xue C, Liu J, Ye X (2025) Triaxial creep characteristics of undisturbed loess under freeze-thaw cycles and its induced landslide mechanism. Acta Geotech 20: 5543–5563.

Liu W, Bai R, Sun X, Yang F, Zhai W, Su X (2024) Rainfall- and Irrigation-Induced Landslide Mechanisms in Loess Slopes: An Experimental Investigation in Lanzhou, China. Atmosphere 15: 14.

Lu X, Jiang Y, Wang N, Shen H (2023) Progressive deformation and failure mechanism of loess fill slopes induce by rainfall: insights from flume model tests. Bull Eng Geol Environ 82: 18.

Ma R, Jiang Y, Liu B, Fan H (2021) Effects of pore structure characterized by synchrotron-based micro-computed tomography on aggregate stability of black soil under freeze-thaw cycles. Soil Tillage Res 207: 10.

Muhs D (2018) The geochemistry of loess: Asian and North American deposits compared. J Asian Earth Sci 155: 81–115.

Nie Y, Ni W, Lü X, Tuo W (2024) Exploring the mechanical behavior and microstructure of compacted loess subjected to dry-wet cycles and chemical contamination. J Rock Mech Geotech Eng 16: 3673–3695.

Niu Z, Xu J, Li Y, Wang Z, Wang B (2022) Strength deterioration mechanism of bentonite modified loess after wetting-drying cycles. Sci Rep 12: 17.

Panin P, Timireva S, Konstantinov E, Kalinin P, Kononov Y, Alekseev A, Semenov V (2019) Plio-Pleistocene paleosols: Loess-paleosol sequence studied in the Beregovoye section, the Crimean Peninsula. Catena 172: 590–618.

Peng S, Zhu C, Zhai L, Xu H, Li Y, Deng G, Ge M, Liu Y (2024) Mechanical response of Q2 loess stratum surrounding a hydraulic tunnel under dry-wet cycles. J Rock Mech Geotech Eng 16: 4955–4970.
Qin B, Li X, Wang L, Gao R, Chai H (2024) Model interpretation and microscopic characteristics of collapsibility evolution of compacted loess under dry-wet cycles. Catena 246: 13.
Saimaiti A, Fu C, Song Y, Shukurov N (2022) Spatial Distribution, Material Composition and Provenance of Loess in Xinjiang, China: Progress and Challenges. Atmosphere 13: 17.
Subramanian S, Ishikawa T, Tokoro T (2017) Stability assessment approach for soil slopes in seasonal cold regions. Eng Geol 221: 154–169.
Sun B, Liu J, Ren F, Li H, Zhang G, Ma J, Ma B, Li Z (2022) Effects of seasonal freeze-thaw and wind erosion on runoff and sediment yields of three loamy slopes of Loess Plateau, China. Catena 215: 14.
Sun J (2002) Provenance of loess material and formation of loess deposits on the Chinese Loess Plateau. Earth Planet Sci Lett 203: 845–859.
Sun S, Liu J, Wei J, Pan C, Fan H, Li K (2025) Understanding the deterioration mechanism of Xiashu loess in dry-wet cycles. Bull Eng Geol Environ 84: 16.
Vasiljevic D, Markovic S, Hose T, Ding Z, Guo Z, Liu X, Smalley I, Lukic T, Vujicic M (2014) Loess-palaeosol sequences in China and Europe: Common values and geoconservation issues. Catena 117: 108–118.
Wang L, Li X, Qin B, Zheng H, Zheng Z (2024) Genesis and evolution mechanism of loess tunnels in the Loess Plateau, China. Catena 239: 18.
Wang X, Hu S, Lian B, Wang J, Zhan H, Wang D, Liu K, Luo L, Gu C (2024) Formation mechanism of a disaster chain in Loess Plateau: A case study of the Pucheng County disaster chain on August 10, 2023, in Shaanxi Province, China. Eng Geol 331: 19.
Wang X, Lu H, Zhang H, Wu J, Hou X, Fu Y, Geng J (2018) Distribution, provenance, and onset of the Xiashu Loess in Southeast China with paleoclimatic implications. J Asian Earth Sci 155: 180–187.
Wang X, Wang J, Zhan H, Li P, Qiu H, Hu S (2020) Moisture content effect on the creep behavior of loess for the catastrophic Baqiao landslide. Catena 187: 12.
Xu J, Li Y, Lan W, Wang S (2019) Shear strength and damage mechanism of saline intact loess after freeze-thaw cycling. Cold Reg Sci Tech 164: 13.
Xu J, Li Y, Wang B, Wang Z, Wang S (2023) Microstructure and Permeability of Bentonite-Modified Loess after Wetting-Drying Cycles. Int J Geomech 23: 12.
Xu J, Ren J, Wang Z, Wang S, Yuan J (2018) Strength behaviors and meso-structural characters of loess after freeze-thaw. Cold Reg Sci Tech 148: 104–120.
Ye W, Li C (2019) The consequences of changes in the structure of loess as a result of cyclic freezing and thawing. Bull Eng Geol Environ 78: 2125-2138.
Ye W, Zhou Z, Bai Y, Guo Z (2024) Multiscale study of the strength deterioration and microstructure changes in loess during dry-wet and freeze-thaw cycles. J Chin Inst Eng 47: 283–292.
Yeon S, Cahill D (2024) Analysis of heat flow in modified transient plane source (MTPS) measurements of the thermal effusivity and thermal conductivity of materials. Rev Sci Instrum 95: 8.

Yuan G, Che A, Tang H (2021) Evaluation of soil damage degree under freeze-thaw cycles through electrical measurements. Eng Geol 293: 13.

Yuan G, Wu Z, Che A, Zhou H (2023) Damage evolution mechanism of loess slope under the combination of freeze-thaw cycles and earthquake. Soil Dyn Earthq Eng 166: 12.

Yuan K, Wang H, Ni W, Ren S, Guo Y (2025) New insights into the dynamic changes of loess collapsibility under climate-induced wetting-drying cycles: A case study of the loess Plateau of China. Catena 250: 17.

Zeng Z, Kong L (2023) Wetting-drying-freezing-thawing cycle effect on the hydro-mechanical behaviour of Yanji swelling mudstone. J Rock Mech Geotech Eng 15: 2746–2756.

Zhang K, Li D, Mu Y, Li G, Wu H, Mao Y, Li L, Zhang Q (2023) Field observations on hydro-thermal regimes of loess cut slopes in cold and arid regions: A comparative study of sunny and shady slopes. Cold Reg Sci Tech 215: 10.

Zhao Z, Zhu Y, Ye S (2025) Experimental study on the failure characteristics of the loess high slope under the coupled effects of soil Consolidation, Rainfall, and evaporation. Eng Fail Anal 171: 15.

Zhi B, Wang S (2024) Mechanical properties and damage mechanism of loess under dry-wet freeze-thaw cycle. Rock Soil Mech 45: 1092–1102.

Zhou G, Xu L, Huang X, Li Y, Zhang H, Dong Y (2023) Synergistic effect of rainfall and pipe leakage erosion on the formation and development of loess caves in Weinan city, Loess Plateau, Northwest China. Environ Earth Sci 82: 18.

Zhuang J, Peng J, Wang G, Javed I, Wang Y, Li W (2018) Distribution and characteristics of landslide in Loess Plateau: A case study in Shaanxi province. Eng Geol 236: 89–96.